Project 074 Low Emission Premixed Combustion Technology for Supersonic Civil Transport

Georgia Institute of Technology

Project Lead Investigator

Adam Steinberg
Associate Professor
School of Aerospace Engineering
Georgia Institute of Technology
Phone: (404) 897-1130
E-mail: adam.steinberg@gatech.edu

University Participants

Georgia Institute of Technology (GT)

- PI: Adam Steinberg, Associate Professor, School of Aerospace Engineering
- FAA Award Number: 13-C-AJFE-GIT-079
- Period of Performance: August 11, 2020 to September 30, 2022
  Period of Performance Covered in Report: October 1, 2020 to September 30, 2021
- Task(s):
  1. Experimental measurement of flame structure, combustion dynamics, and emissions
  2. Large-eddy simulations (LES) of combustor operation and emissions

Project Funding Level

FAA: $1,999,998
Georgia Institute of Technology: $1,000,262
GE Research: $999,736

Investigation Team

Name	Affiliation	Role	Tasks
Adam Steinberg Associate Professor	Georgia Institute of Technology	PI	Management, reporting, technical oversight of all tasks, oversight of optical diagnostics in Task 1
Ellen Mazumdar Assistant Professor	Georgia Institute of Technology	Co-PI	Oversight of non-volatile particulate matter (nvPM) measurements in Task 1
Joseph Oefelein Professor	Georgia Institute of Technology	Co-PI	Oversight of first-principles LES in Task 2 and overall coordination of Task 2
Jerry Seitzman Professor	Georgia Institute of Technology	Co-PI	Oversight of gas-phase fuel/air mixing diagnostics in Task 1
Michael Benjamin Consulting Engineer	GE Aviation	Co-PI	Oversight of combustor design in Task 1, coordination of GT/GE LES collaboration in Task 2
Krishna Venkatesan Principal Engineer	GE Research	Co-PI	Oversight of combustor operation in Task 1

Oleksandr Bibik **Senior Research Scientist**	Georgia Institute of Technology	Participant	Task 1
Hannah Bower **Research Engineer**	GE Research	Participant	Task 1
R. Narasimha Chiranthan	GE Aviation	Participant	Task 2
Manampathy Giridharan	GE Aviation	Participant	Task 2
Hiranya Nath	GE Aviation	Participant	Task 2
John Hong **Lead Engineer**	GE Research	Participant	Task 1
Sriram Kalathoor **Graduate Research Assistant**	Georgia Institute of Technology	Graduate Student	Task 2
Mitchell Passarelli **Graduate Research Assistant**	Georgia Institute of Technology	Graduate Student	Task 1
Samuel Wonfor **Graduate Research Assistant**	Georgia Institute of Technology	Graduate Student	Task 1
Andrew Zheng **Graduate Research Assistant**	Georgia Institute of Technology	Graduate Student	Task 1
Kailey Obenstine **Research Assistant**	Georgia Institute of Technology	Undergraduate Student	Task 1
Coleman Pethel **Research Assistant**	Georgia Institute of Technology	Undergraduate Student	Task 1
Rachel Thomas **Research Assistant**	Georgia Institute of Technology	Undergraduate Student	Task 1

Project Overview

The market demand for high-speed transport is expected to drive a rapid re-emergence of commercial supersonic transport (CST) aircraft over the coming decades. This impending CST revival, combined with the increasingly harmful impacts of anthropogenic climate change, mandate advancements in CST-focused environmentally compatible technologies and policies. Compared with subsonic aircraft, engines for CST aircraft will (a) operate at significantly lower overall pressure ratio (OPR) and bypass ratio (BR); (b) experience higher combustor inflow temperatures (T_3), lower pressures (p_3), and higher fuel/air ratios at cruise; and (c) cruise at higher altitudes. The reduced OPR and BR result in increased thrust-specific fuel consumption, thus increasing fuel burn and making emission reductions fundamentally more challenging. Furthermore, the combination of a low OPR and high cruise T_3 and FAR result in complicated trade-offs between nitrous oxide (NO_x) at cruise and other emissions (CO, nonvolatile particulate matter [nvPM] and unburnt hydrocarbons [UHC]) at lower power.

Several recent studies have assessed potential CST fleet emissions and environmental impacts based on currently deployed rich-burn–quench–lean-burn combustors (typically Tech Insertion combustors) designed for subsonic transport (Berton et al., 2020; Speth et al., 2021; Hassan et al., 2020; Kharina et al., 2018). These studies have demonstrated that innovations in combustor architecture will be required to meet emission targets and to create an environmentally compatible CST market. Despite the high T_3 and FAR, peak flame temperatures must be moderated to meet NO_x targets, while also maintaining efficiency and achieving low CO, UHC, and nvPM levels, which will require increased fuel-lean premixing prior to combustion.

Lean premixed pre-vaporized (LPP) combustors are a promising path to lowering emissions from future CST engines. In LPP combustors, fuel is injected, partially pre-vaporized, and partially premixed with air before the reactants enter the combustor. While the LPP concept is not new, e.g., (Niedzwiecki, 1992), achieving good vaporization and mixing in a flight-appropriate package has been challenging in the past. However, these issues can potentially be alleviated by the high T_3 in CST combustors—which results in faster vaporization—and advanced manufacturing to enable compact rapid-mixing flow elements.

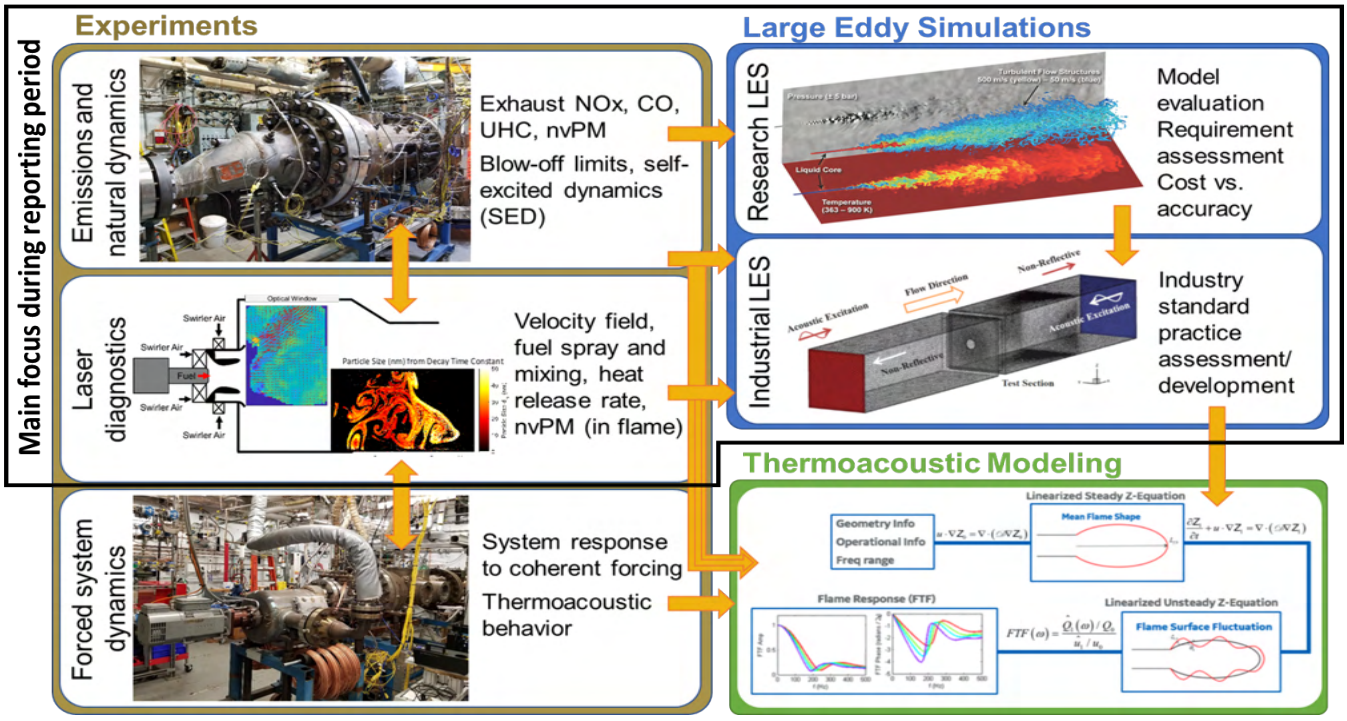

Figure 1. Project overview.

Thus far, the ability of current design methodologies to predict the operability and emissions of LPP combustors under relevant conditions is unproven. Hence, there is a critical need to generate high-quality experimental data under CST combustor conditions, coupled with the development/validation of computational fluid dynamics (CFD) simulations and reduced-order thermoacoustic models. This project will fill this need through a combination of experiments, LESs, and thermoacoustic modeling, all applied in a novel LPP combustor of interest to future CST applications. Figure 1 shows the elements of this research project. Note that the Period of Performance covered in this report focuses on the experiments and LESs.

Task 1 – Experimental Measurements of Flame Structure, Combustion Dynamics, and Emissions

Objective(s)

This task represents the experimental efforts involved in measuring the flame structure, dynamics, and emissions in a novel LPP combustor concept, designed specifically for low-emission operation under typical conditions encountered by CST engines.

Research Approach

Efforts under Task 1 over the reporting period consisted of four main activities.

1) Design, fabrication, and deployment of the LPP combustor in a test cell at GE Research.
2) Design and calibration of optical diagnostics using a high-pressure laminar flame burner at Georgia Tech, with associated student training.
3) Experimental Campaign 1, in which optical diagnostics from Georgia Tech were transported to GE Research and deployed in the LPP combustor test cell, along with emission diagnostics provided by GE. Three Georgia Tech students were onsite at GE Research for a total of nearly 9-person months over the summer of 2021 to conduct this experimental campaign in collaboration with GE staff.
4) Analysis of experimental data from Campaign 1.

Experimental Design, Fabrication, and Calibration

Considerable preliminary work was performed to enable on-schedule completion of Experimental Campaign 1. The following major elements of the test rig at GE Research were designed and fabricated:

1) LPP combustor,
2) Combustor dome face,
3) Test rig spool piece,
4) Water-cooled emission probe,
5) Window blank with pressure measurement ports, and
6) Custom laser cart and optical tables.

Significant effort was required to optimize the optical layout of the diagnostics due to space constraints in the test cell, safety considerations, and the need for routine access to the test article. The resultant optical layout is described in detail below.

Concurrent with these activities, a high-pressure laminar flame burner (shown in Figure 2) was deployed at Georgia Tech for the purpose of calibrating the various laser diagnostics. Specifically, it was necessary to calibrate the time-resolved laser-induced incandescence (TiRe-LII) diagnostics for accurate measurements of nvPM primary particle size and the fuel planar laser-induced fluorescence (PLIF) diagnostics to account for laser absorption and oxygen quenching. The efforts described in this report pertain to the calibration and evaluation of TiRe-LII measurements. This burner is capable of stabilizing premixed flames of pre-vaporized Jet A fuel and air over lean and rich equivalence ratios and pressures up to 10 bar. Multiple windows were included to provide optical access for laser diagnostics.

The measurement model for TiRe-LII is described below. To calibrate the TiRe-LII model for quantitative nvPM primary particle size measurements, it is necessary to perform TiRe-LII and extractive nvPM sampling under the same conditions. Subsequently, the sampled measurements can be analyzed using transmission electron microscopy (TEM) to provide detailed quantification of the primary particle size, aggregate structure, and other nvPM properties. These properties can then be compared with the TiRe-LII signals to calibrate the measurement model.

Hence, an extractive sampling system, leveraging thermophoresis, was created to sample nvPM from this flame (Vargas & Gülder, 2016). This system contains eight TEM grids that are rotated into the flame to precisely control sampling times using a stepper motor. Samples that are deposited onto the grids are analyzed using a Tecnai F30 300 kV HR TEM, producing images of the nvPM such as those shown in Figure 3. Previously established post-processing routines are then applied to characterize the nvPM, such as the distribution of primary particle sizes, which can be used to calibrate the TiRe-LII.

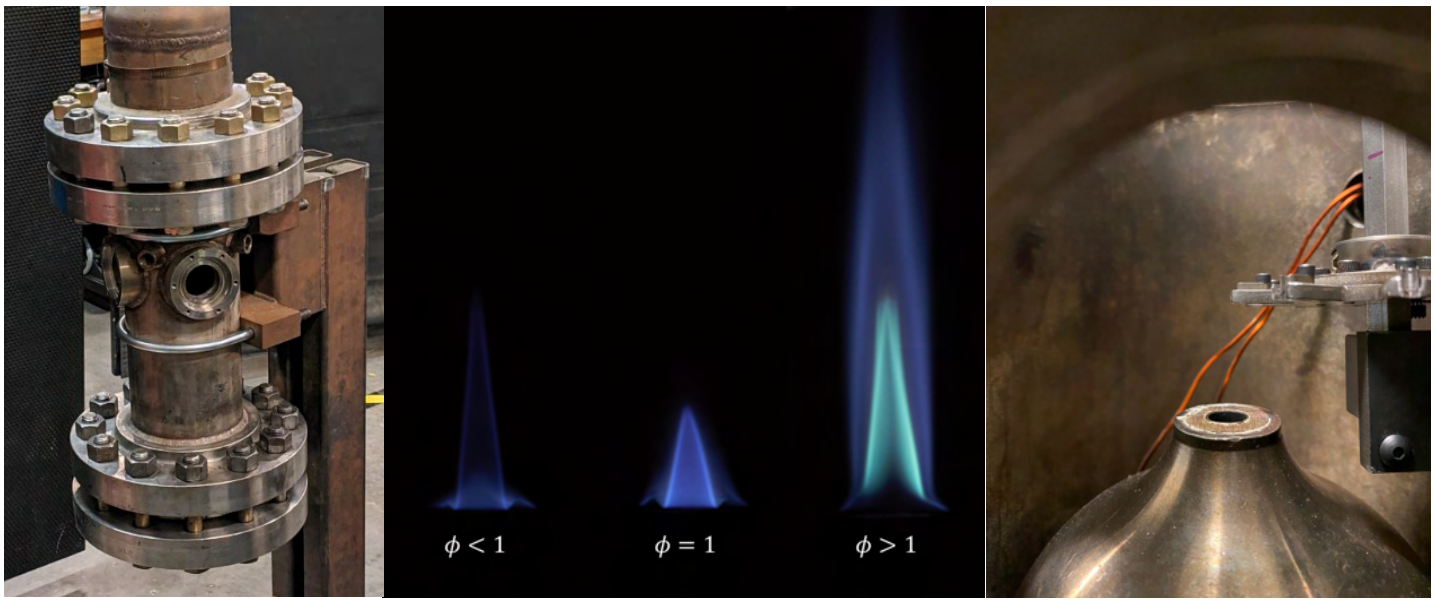

Figure 2. High-pressure calibration burner. Left: Pressure vessel. Middle: Typical laminar flames at different equivalence ratios. Right: Thermophoretic nvPM sampling system.

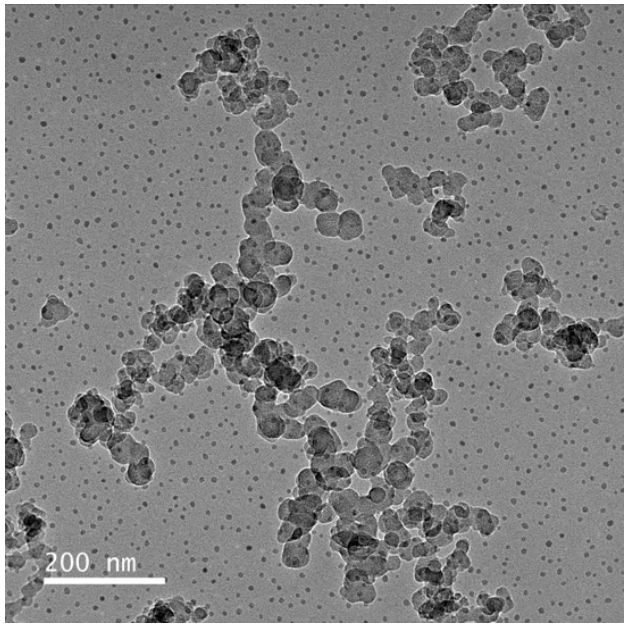

Figure 3. Typical TEM image of sampled nvPM.

The TiRe-LII model is used to fit measured incandescence intensity decay curves to a primary particle size. The baseline model is based on work by Liu et al. (2005) and includes laser absorption, conduction, and radiation elements with control volumes placed around soot particles or soot agglomerates, as shown in Figure 4. For lower laser fluences, the dominant heat transfer mechanism is conduction, which can occur in the free molecular regime or the continuum regime as a function of the Knudsen number. To accurately incorporate temperature-dependent thermal conductivity terms, temperature-dependent specific heat terms, and conduction regimes, an iterative solver was implemented. At higher laser fluences, sublimation mechanisms begin to play a larger role in the incandescence signals. For this project, we incorporated the sublimation mechanisms proposed by Michelson et al., 2007, which account for changes in mass and particle diameter. These differential equations are then solved simultaneously to determine decay profiles as a function of particle size and flame conditions. Once the temperature profiles are determined, the data are converted to light using Planck's equation.

For preliminary TiRe-LII model fitting, a simple procedure was devised that first forward-simulates decay profiles for several different soot particle sizes using low laser fluences. These temperature profiles are then converted to intensity profiles. Because these intensity profiles have a roughly first-order exponential decay, time constants can be derived from each decay profile. From these data, a soot particle size to decay time constant library can be developed for each operating condition (bath gas temperature, pressure, etc.).

Initial validation of these data focused on estimating soot particle sizes from laminar and turbulent non-premixed ethylene flames operating at atmospheric pressure (Chen et al., 2018; Shaddix et al., 2010). The data for these calibrations were collected with a 1064-nm laser, a bandpass filter (640 ± 75 nm), and a Shimadzu HPV-X2 ultrahigh-speed camera (10-MHz acquisition, 50-ns exposure). Utilizing published values for soot aggregate size and bath gas temperature (1850 K for the laminar flame and 1628 K for the turbulent flame), we were able to fit our model library data to the incandescence decay at each pixel. These preliminary estimates match well with literature values and show a clear difference in particle size in the nvPM growth region versus the soot oxidation region. The next step in this effort is to generate more accurate calibrations of nvPM particle size at relevant pressures and temperatures using the aforementioned laminar flame burner and extractive sampling system. This step will help to improve model estimates and reduce estimation uncertainties.

Experimental Campaign 1

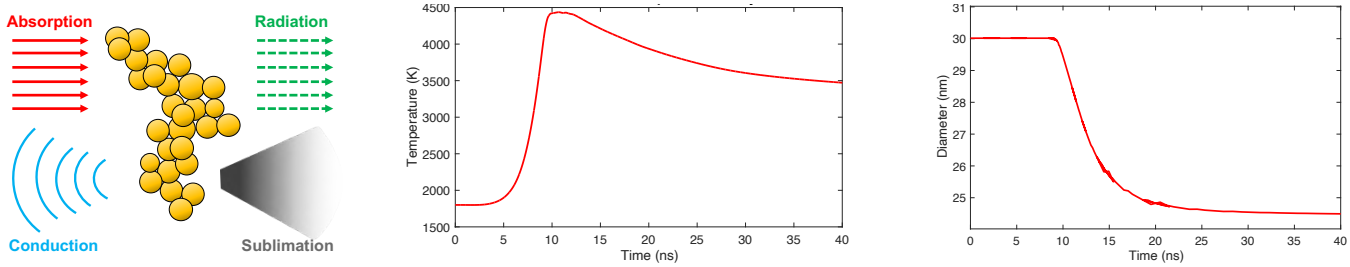

(a) (b) (c)

Figure 4. (a) Soot incandescence decay models showing changes in (b) particle temperature and (c) particle diameter after laser incidence.

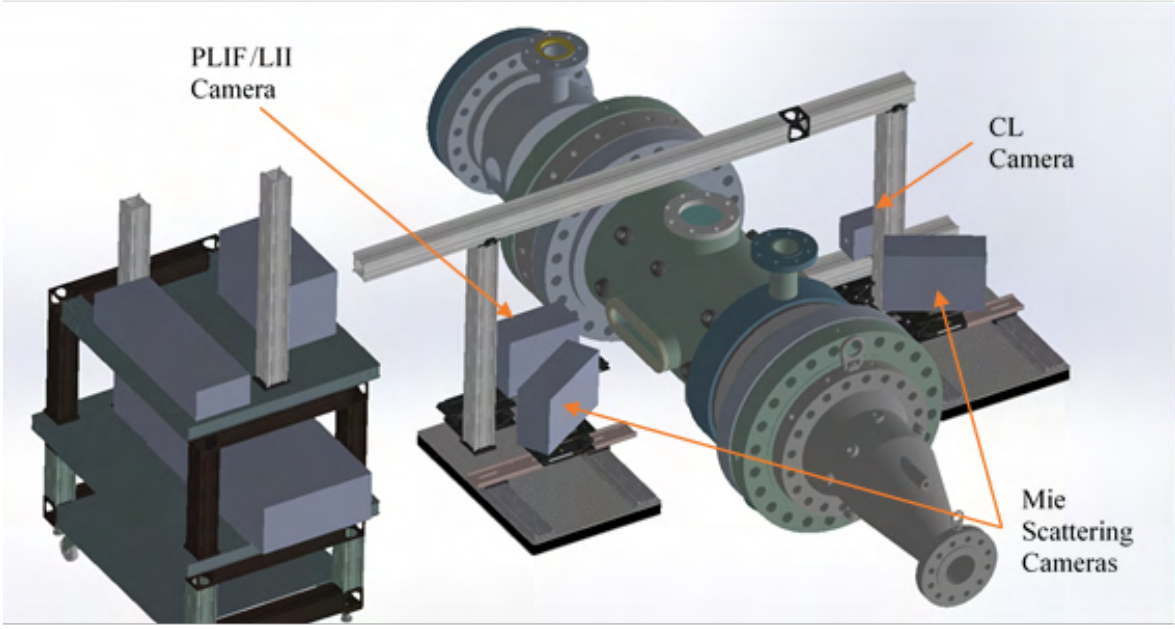

Figure 5. Test cell schematic with optical diagnostics.

Combustor & Operating Conditions: Experiments were performed at GE Research in Niskayuna, New York. Figure 5 shows the facility used for the experiments and the layout of the optical diagnostics. Figure 6 shows a schematic of the combustor dome face, which consists of four bluff-body stabilized "main" flames surrounding a central swirling pilot flame. Note that the bluff-body geometry is redacted. Each main flame operates under fuel-lean conditions, burning partially pre-vaporized and premixed Jet A fuel. For the majority of the laser diagnostics described below, the laser sheet passes through the centers of the main flames on one side of the combustor, as indicated in Figure 6.

Experiments were performed for a wide range of conditions (p_3, T_3, and FAR) relevant for CST operation. For the optical data presented in this report, each test point was acquired at the same air preheat temperature, $T_3 = 7.0 \times 10^2$ K, and a pressure appropriate for nominal cruise of a CST engine. Normalized emission data are also presented for different p_3 and T_3 combinations. For each test case, the FAR was varied, resulting in a sweep of the combustor exit temperature, T_4. Prior to data acquisition, the combustor was allowed to settle to steady state, as verified by an examination of static pressure, thermocouple, and mass flow rate measurements.

Diagnostics: Chemiluminescence (CL) imaging of OH* at 308 ± 5 nm served as the metric for line-of-sight integrated heat release rate measurements. Previous experiments (Kheirkhah et al., 2017) and wide-spectrum measurements from a portable spectrometer (Ocean Optics HR2000) showed that OH* is the most appropriate indicator of heat release rate. A sample spectrum is shown in Figure 7, with the peak corresponding to OH* emissions indicated. CL images were recorded at 10 kHz using a high-speed camera (Photron SA-5) coupled to an image intensifier (Invisible Vision UVi 2550B-10, gate time of 50 μs), commercial objective lens (Nikkor 105 mm UV, f/# = 11), and bandpass filter (312 ± 12.5 nm).

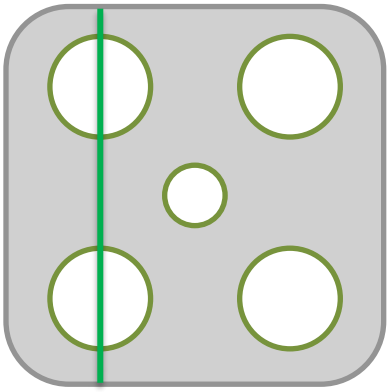

Figure 6. Combustor geometry, with the laser sheet position indicated by a green line. The four corners contain the partially premixed bluff-body stabilized main flames. The bluff-body geometry has been redacted.

Qualitative measurements of the fuel spray and mixing behavior were obtained via fuel droplet Mie scattering and PLIF of the aromatic species naturally present in the Jet A fuel, respectively. The flow was illuminated at a repetition rate of 10 Hz using the second (532 nm) and fourth (266 nm) harmonic outputs of a Nd:YAG laser (Spectra Physics Quanta-Ray PRO 350). The 532-nm beam was obtained from the residual of the fourth harmonic generator and was used for fuel droplet Mie scattering, while the 266-nm beam was used for PLIF. Both beams were formed into sheets of similar size via three separate cylindrical-lens telescopes, and were oriented perpendicular to the combustor dome face.

The Mie scattering was collected using two cameras (Phantom v2640) in a forward-scatter configuration with Scheimpflug adapters (LaVision), objective lenses (Tamron 180 mm, f/# = 8), and bandpass filters (532 ± 5 nm). Only one of the cameras was used for the analysis presented here because both cameras were qualitatively similar. The 532-nm sheet had a beam waist of approximately 2 mm at the midplane in the test article.

Laser-induced fluorescence was collected using an intensified camera (Andor iStar sCMOS, gate time of 100 ns) with an objective lens (Nikkor 105 mm UV, f/# = 4.5) and a two-filter setup consisting of a bandpass filter (340 ± 40 nm) and a steep-edge long wave pass filter (325 ± 3.5 nm). This filter setup aligned with the center of the fluorescence spectrum of kerosene vapor [13] while simultaneously blocking the signal from OH* CL. Simultaneous shot-to-shot beam profile measurements were made by using a cuvette filled with a rhodamine dye solution. The cuvette was placed in the path of residual transmission from the 266-nm sheet through the final mirror above the combustor at a point such that the beam waist was formed. This low-intensity copy of the sheet within the combustor induced visible fluorescence within the dye solution, which was then imaged with a separate camera system (FLIR Blackfly USB3).

Single-camera, single-laser shot two-dimensional TiRe-LII (Chen et al., 2019) was performed to analyze nvPM along the centerlines of the pilot and main flames. A 10-Hz, 1064-nm laser (Quanta-Ray PRO-350) was used to heat nvPM in the flame, and incandescence decay was captured along a 30-mm-long, 2-mm-thick laser sheet (fluence of 0.08 J/cm^2). The decay was captured at 10 MHz using an ultrahigh-speed camera (Shimadzu HPV-X2, 50-ns exposure) through an objective lens (85 mm, f/# = 1.4) and a bandpass filter (640 ± 75 nm) to block CL and laser illumination. Note that the LII measurements were not performed simultaneously with the fuel PLIF; thus, the results presented in this paper correspond to different test cases. A schematic of the TiRe-LII optics is shown in Figure 8, although this does not reflect the actual geometric arrangement of the optics deployed in the test cell (Figure 5).

Pressure fluctuations were measured using dynamic pressure transducers (PCB), mounted to the ends of calibrated waveguides in a semi-infinite loop configuration at three axial locations within the combustor. A data acquisition system (National Instruments USB-6361) recorded the pressure and camera timing signals at a sampling rate of 100 kHz. All three pressure measurements were qualitatively identical; thus, the data from the middle transducer were used for subsequent spectral analysis. Spectral analysis of the pressure and CL indicated that there were no significant natural thermoacoustic dynamics in the combustor.

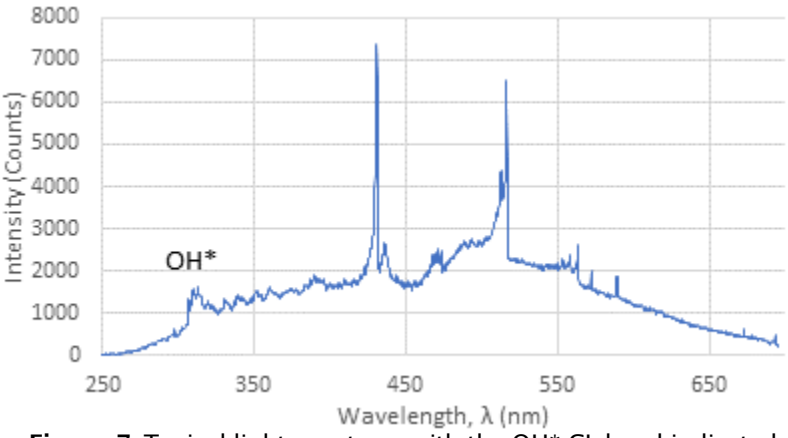

Figure 7. Typical light spectrum with the OH* CL band indicated.

Combustor emissions were measured using an axially and radially traversable water-cooled probe. Several analyzers were used to detect UHC (CAI model 600 HFID), CO/CO_2 (CAI model 603 NDIR), and nitrous oxide (CAI model 600 HCLD).

Optical Data Processing: Prior to analyzing the fuel spray Mie scattering data, the images were preprocessed to both correct the visual perspective and remove the background in the images. For the perspective calibration and correction, LaVision's DaVis 8.4 was used with a third-order polynomial model based on images taken of a LaVision 106-10 two-sided, two-plane calibration plate.

Due to the largely pre-vaporized nature of this combustor, few droplets were present in the combustor. This resulted in relatively low signal-to-noise in the Mie scattering data, necessitating considerable processing to extract meaningful information about the residual fuel spray. Figure 9 illustrates the processing pipeline. First, a mask was applied to the images to exclude regions without droplets. All images were then normalized to the same mean intensity to account for variations in pulse energy across all frames. Subsequent processing using a temporal high-pass filter removed the quasi-static background associated with the flame and laser reflections. Finally, thresholding and image segmentation operations removed much of the leftover background noise passing through the filter and identified the spray field in the combustor.

The PLIF images were processed for spatial calibration, background removal, intensifier white-field response, and shot-to-shot laser sheet intensity and profile variations, where the laser sheet profiles were extracted from images taken by the aforementioned cuvette–camera system. At present, no corrections have been made for the absorption of laser power through the domain or fluorescence quenching, although such corrections will be implemented in the future once calibration data are acquired.

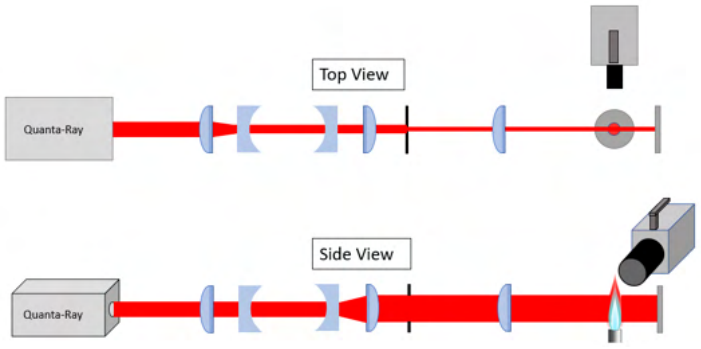

Figure 8. Schematic of TiRe-LII laser sheet forming optics.

Preprocessing for LII data began with background removal from each dataset. Each dataset was also spatially calibrated with calibration images taken before each test. To generate average prompt LII images, prompt LII images from each dataset were extracted for each test point condition and averaged. The intensity of each averaged image in the ramp-up condition set was averaged to the same baseline intensity determined from the intensity range of the ramp-up condition dataset. Because the datasets taken from full operating conditions had a lower signal overall, they were normalized to 1/10th of the baseline intensity. Each dataset was then fitted to obtain decay times for each pixel. However, due to the sparse amount of nvPM detected, fast intensity decay times in the datasets, and lack of a calibrated LII model for Jet A, particle-sizing abilities were limited.

Each TiRe-LII dataset was preprocessed by first referencing the coordinate system to spatial calibration plates. Then, the incandescence emission background for each dataset was removed. To generate average prompt LII images, which serve as

an estimate for soot volume fraction, the first frame after laser arrival from each dataset was extracted and grouped by test condition. To estimate soot particle sizes, the time profile for each pixel is examined, and only pixels above a certain brightness threshold are selected. The time profiles of these pixels are then fit to exponential decays to determine the particle time constants, which can be further correlated to particle sizes using LII modeling techniques.

Results & Discussion

Figure 10 shows the NO_x and CO emission trends for this combustor. Note that "NC" in Figure 10 designates "nominal cruise" pressure conditions. The increase in CO emissions observed for lean FAR (low combustor exit temperature) indicates that the system is approaching lean blowout (LBO). Each data series corresponds to a different T_3 range, as indicated in the legend. The series indicated by the yellow "x" markers matches the test cases for the optical data presented below. While quantitative values cannot currently be published, the maximum NO_x values are in line with NASA's 2035 CST goal (NASA, 2019).

To analyze the fuel spray and mixing characteristics, the mean fuel droplet Mie scattering, OH* CL, and fuel PLIF fields were computed for each test case. The mean fields are shown in Figure 11, with each case (columns in Figure 11) ordered from left to right by decreasing FAR. Each set of mean fields (corresponding to each row in Figure 11) is normalized by the maximum intensity across all cases. The spatial coordinates for the spray Mie scattering and fuel PLIF fields are normalized by the outer diameter of the main fuel injectors. Note that the spray and PLIF field of view are smaller than the OH* CL field of view. The red rectangle in the first CL mean field indicates the approximate position of the Mie scattering and PLIF fields of view.

1) Raw Images | 2) Mask & Intensity Normalization | 3) Perspective Correction & Cropping | 4) Temporal Butterworth High-pass Filter | 5) Thresholding & Image Segmentation

Figure 9. Post-processing pipeline for Mie scattering.

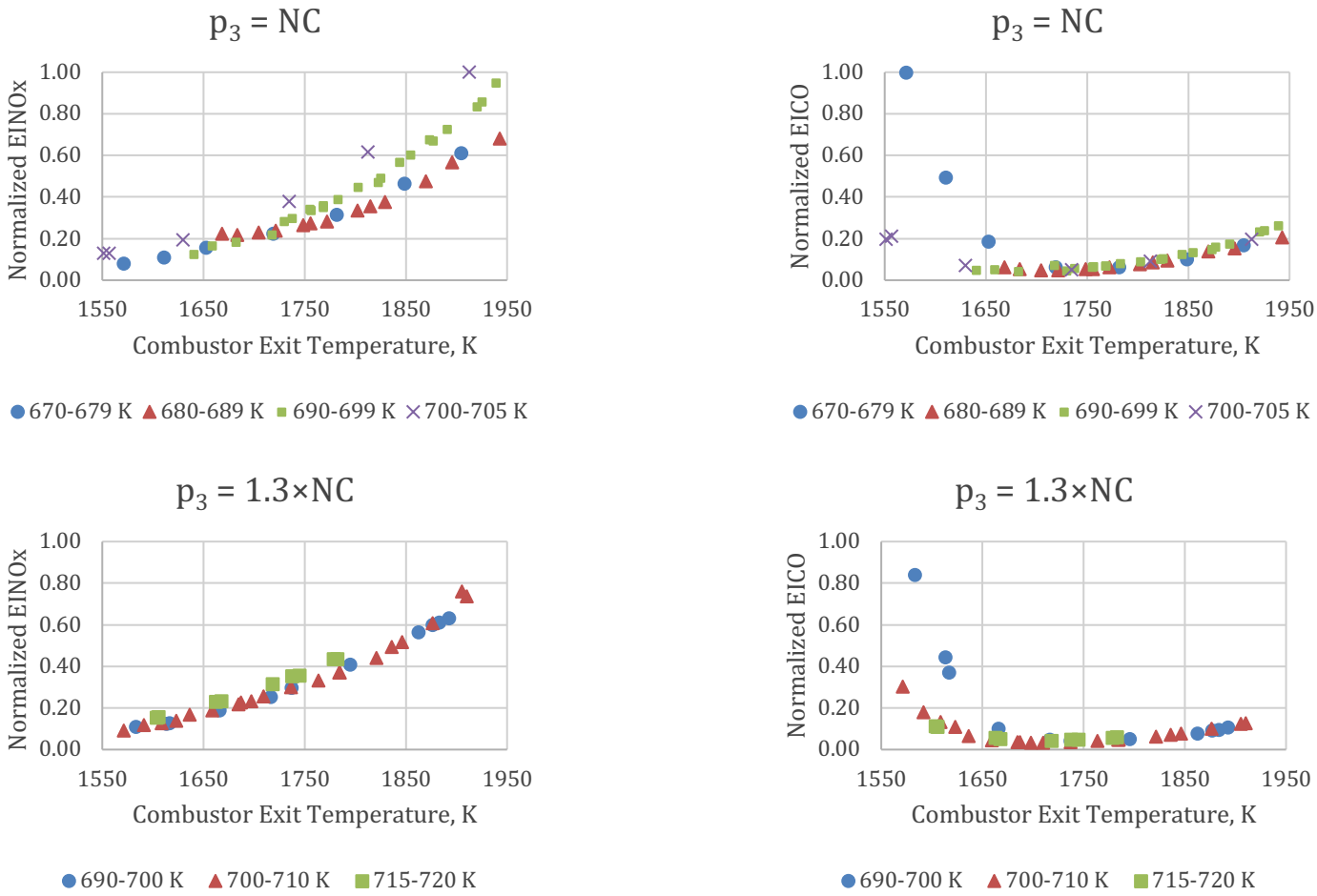

Figure 10. Normalized emission indices over several test points. The top row corresponds to nominal pressure conditions, and the bottom row corresponds to higher pressure. NC: nominal cruise.

Despite the sparsity of fuel droplets in the spray, the Mie scattering mean fields generally agree with the results in the PLIF mean fields in terms of length and qualitative intensity between regions. The sparsity of fuel droplets also indicates that the combustor is vaporizing most of the fuel prior to entry into the combustion chamber, resulting in good overall mixing. Differences in the mean fuel amount between the mains (and between the two halves of each main) may be attributed to the discrete fuel injectors in the premixer tube and other naturally arising asymmetries.

For higher FARs, the fuel PLIF measurements show an annular region of premixed fuel and air, as well as regions of low PLIF signals denoting burnt products. Product gases occurred both within the bluff-body recirculation zone and surrounding the fuel/air jets, indicating an annular partially premixed flame surface. Decreasing the FAR from Case 1 to 4 decreased the PLIF and OH* signals without qualitative changes in the flame geometry. For Case 5, the lower flame blew out, resulting in the lack of a lower main flame in the OH* CL; thus, premixed fuel and air filled the recirculation zone in the PLIF images. In Case 6, there was a complete blow out of the main flames. It is worth noting that the behavior of the main fuel injectors was not symmetric in the direction perpendicular to the laser sheet. Specifically, in Case 5, the upper main on the side of the combustor opposite the laser sheet had also blown out (three of the four mains were blown off). The relatively high root-mean-squared fuel PLIF fluctuations for all conditions are indicative of a high turbulence intensity in the shear layer between the mains and recirculation zones, as well as spatiotemporal variations in the fuel/air mixing exiting the premixer tubes. A comparison of Figures 10 and 11 shows that the observed increase in CO with decreasing FAR corresponds to the conditions approaching LBO.

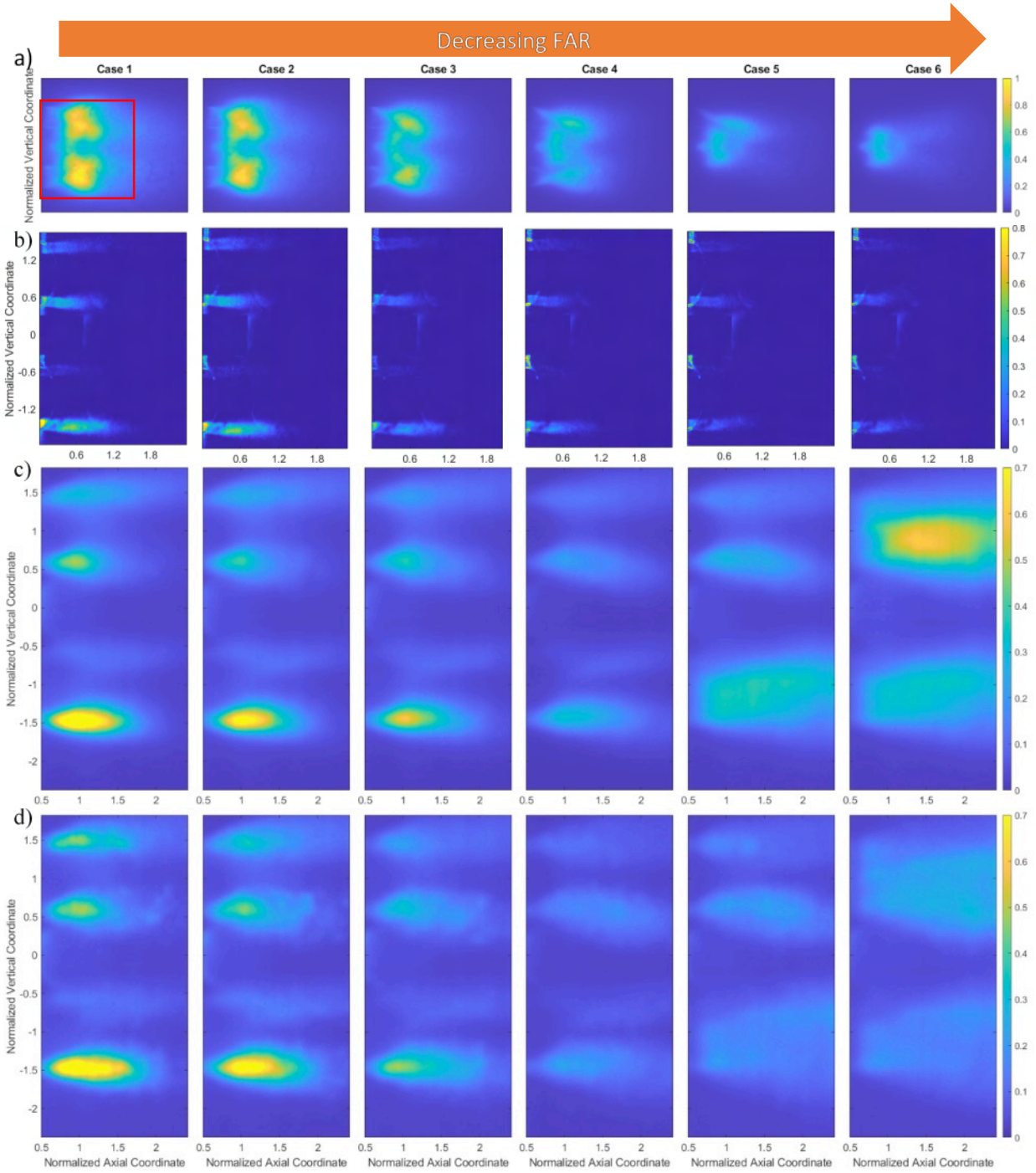

Figure 11. (a) Mean OH* CL, (b) mean fuel droplet Mie scattering, (c) mean fuel PLIF, and (d) fuel PLIF root-mean-squared fluctuations. The approximate position of the spray and PLIF field of view is denoted by a red rectangle in the first OH* field.

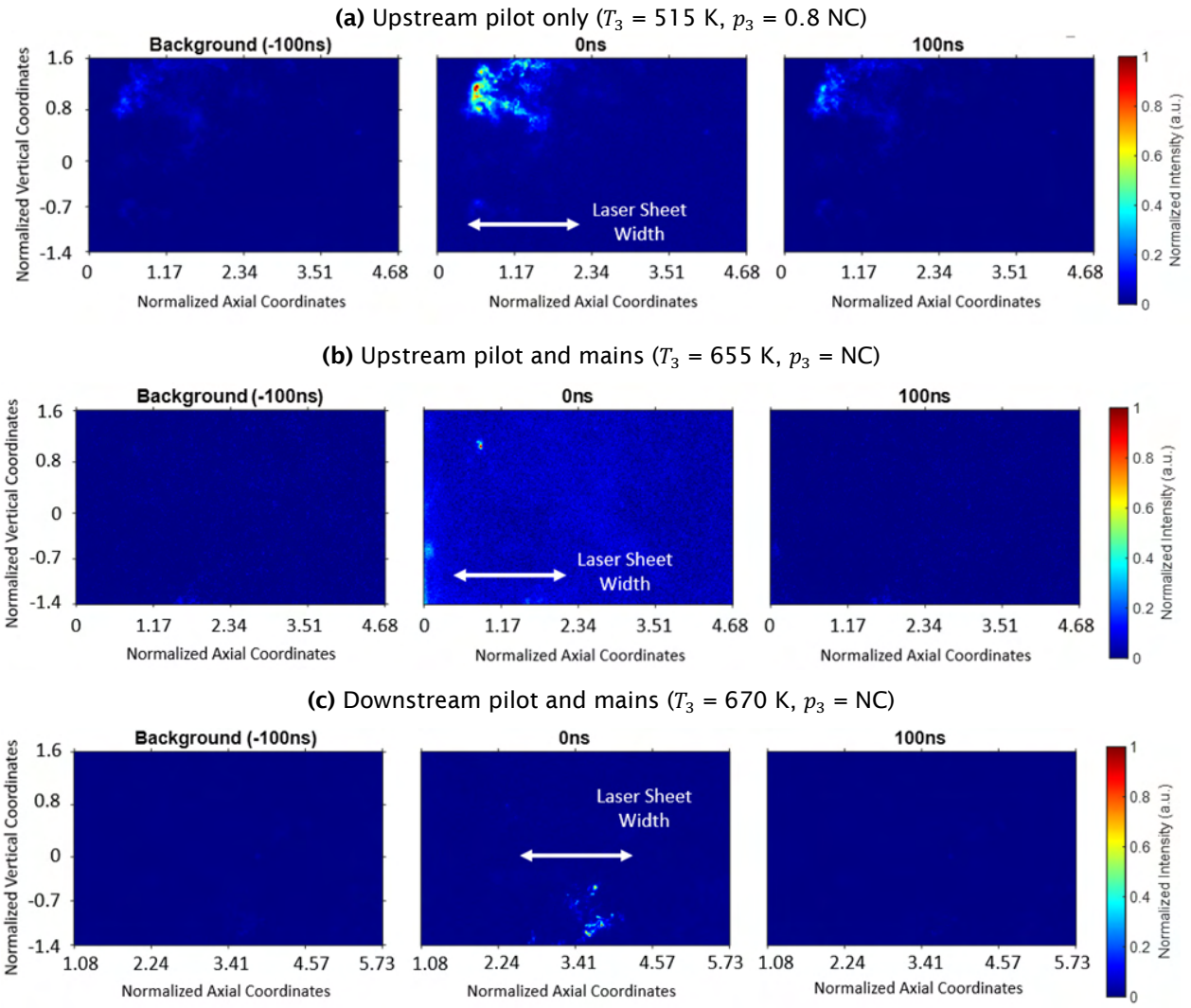

Figure 12. Ultrahigh-speed video sequences showing soot incandescence for different conditions and locations inside the combustor. NC: nominal cruise.

Typical TiRe-LII image sequences collected by the ultrahigh-speed camera are shown in Figure 12. Here, a background image is displayed immediately before the laser pulse arrives, which is rapidly followed by a prompt LII signal and the incandescence decay at 100 ns after laser incidence. The pilot-only operating condition at lower temperatures and pressures shows significant soot production near the dome face with relatively fast decay times, on the order of 78.5 ns. As the pressure and temperature are increased and the mains are turned on, the soot production near the dome face drops significantly, with isolated areas of soot production. The soot incandescence decay time also decreases significantly to approximately 12.4 ns. However, downstream from the dome face, more soot particles can be measured with slightly longer decay times on the order of 26.3 ns.

The TiRe-LII data collected in both upstream (combustor dome face) and downstream (approximately two main diameters downstream of the dome face) sections of the combustor can be compiled to produce estimates of average, rather than instantaneous, soot production images. Data collected under ramp-up conditions near the interaction region between the pilot and mains indicated clouds of soot with short decay times ranging from 50 to 150 ns. However, for full operating

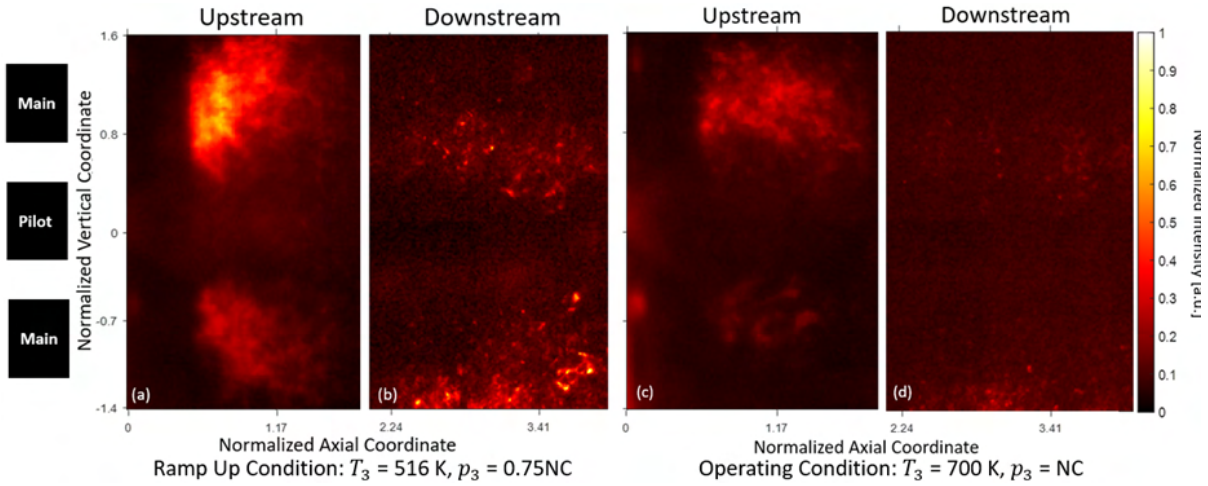

Figure 13. Upstream and downstream average (approximately 100 shots) prompt LII images are shown for ramp-up and operating conditions in (a)–(d). The relative intensities for (a) and (b) are normalized to the same baseline intensity, while those for (c) and (d) are normalized to 1/10th of the baseline intensity. NC: nominal cruise.

conditions, the flame was bluer, and significantly less soot was detected in both the upstream and downstream regions. For the small amounts of intermittent soot measured in the downstream location, the decay times were extremely short (approximately 30 ns) with high uncertainties, limiting particle-sizing capabilities. Average prompt LII images illustrate the decrease in soot detected between ramp-up and operating conditions. Upstream and downstream data taken under similar ramp-up and operating conditions (Figure 13) show an overall decrease in the LII signal across both upstream and downstream regions as the combustor pressure and temperature increased. While the upstream and downstream images are calibrated to be at the same vertical location, the downstream images appear to be shifted down due to variations in combustor height along the axial direction and thermal expansion effects. Despite this shift between cases, the differences between the ramp-up and full operating conditions are apparent, as shown in Figure 13. Here, the prompt LII signal for the operating condition is 1/10th as bright as that for the ramp-up conditions. Examples of signal decay profiles for both the ramp-up and operating conditions are shown in Figure 14.

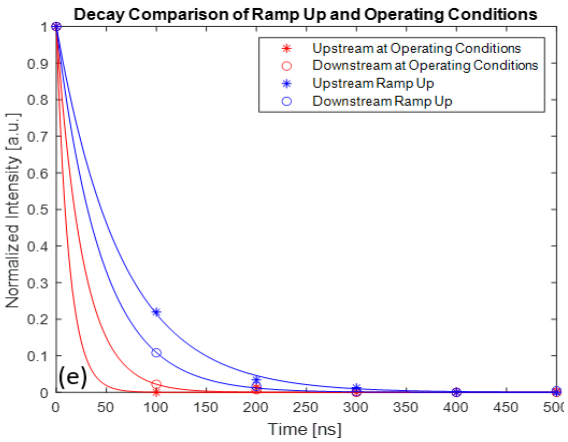

Figure 14. Typical signal decay times for ramp-up and operating conditions.

Because there is significantly more data for ramp-up conditions and the decay time constants for these conditions are longer, it is possible to examine how T_3, p_3, and ϕ affect the production of soot. Figure 15 shows average prompt LII images collected for several different ramp-up conditions. Here, a decrease in pilot ϕ appears to reduce the average soot production. Similarly, increases in temperature and pressure result in a significantly reduced signal from soot incandescence, indicating lower soot volume fractions.

The incandescence decay time constants can also be extracted from these data for each pixel, as illustrated in Figure 16. Here, two test cases are shown, one (Case A) with a lower T_3 and p_3 and a higher ϕ and a second (Case B) with a higher T_3 and p_3 and a lower ϕ. Here, despite the sub-frame decay times, clear differences can be noted between the low and high pressure and temperature conditions. The time constants fit to Case A (peak of distribution at 35 ns) have a larger time constant distribution than Case B (peak of distribution at 28 ns). These findings indicate that increasing temperature, increasing pressure, or decreasing ϕ will likely produce soot with faster decay time constants. To accurately determine how this trend affects soot particle sizes, more work is needed to calibrate the TiRe-LII models at higher pressures.

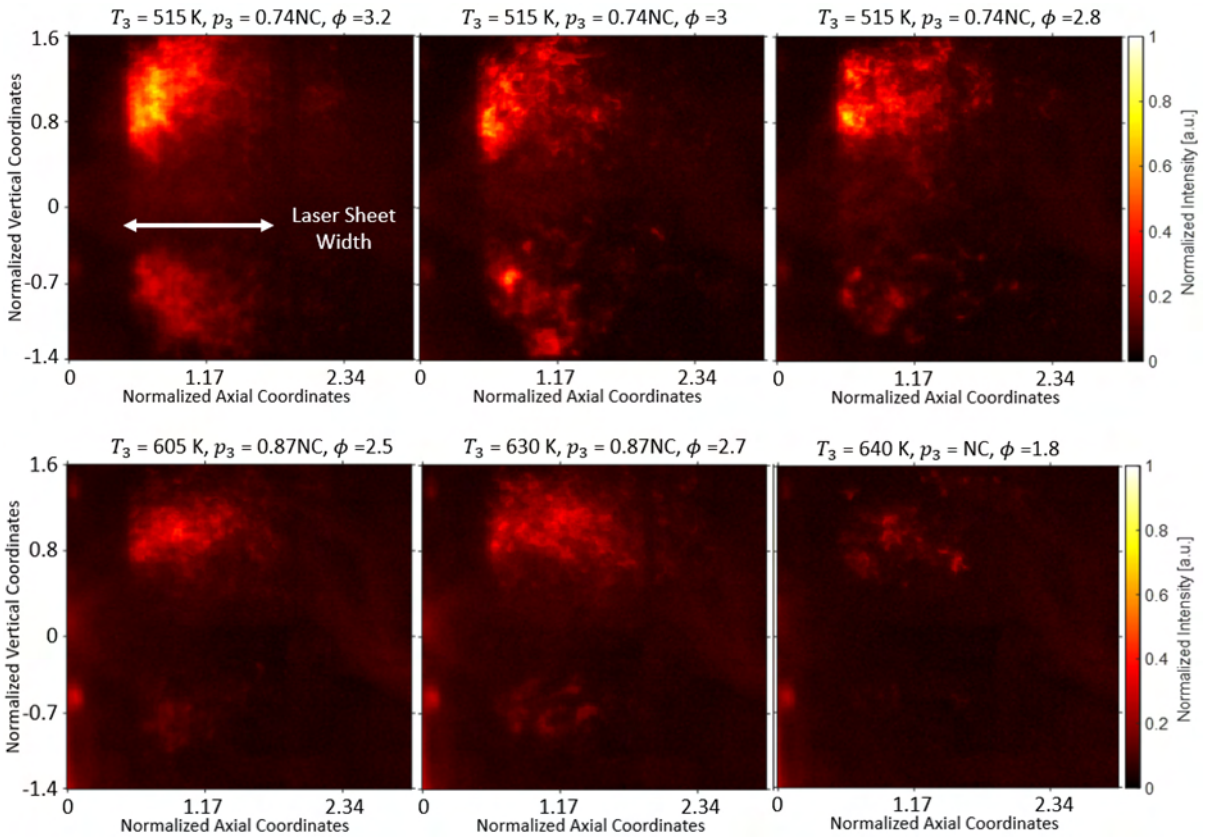

Figure 15. Average (approximately 100 shots) prompt LII images for different ramp-up conditions in which only the pilot flame is operating. NC: nominal cruise.

Milestone(s)

- Campaign 1 test rig design (complete)
- Measurement system design (complete)
- Campaign 1 test rig fabrication (complete)
- Experimental Campaign 1 (complete)
- Data processing from Campaign 1 (on schedule for completion in Q1 2022, 80% complete)
- Campaign 2 test rig design (on schedule for completion in Q1 2022, 50% complete)

Major Accomplishments

- Design, fabrication, deployment, and operation of a novel LPP combustor
- Advancement of various optical diagnostics for high-pressure gas turbine conditions
- Emission and optical measurements demonstrating encouraging performance for CST-relevant conditions

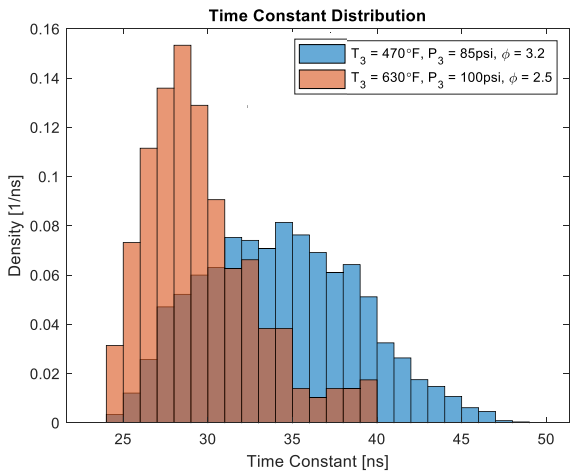

Figure 16. Time constant distributions for two different ramp-up conditions in which only the pilot flame is operating.

Publications

Passarelli, M., et al. (2022). *Experimental characterization of a lean pre-vaporized premixed combustor for supersonic transport applications.* Manuscript accepted for presentation.

Outreach Efforts

Eight semesters of undergraduate research-for-credit have been associated with this project.

Awards

None

Student Involvement

Mitchell Passarelli (PhD Candidate), Georgia Tech: Mie scattering and OH* CL measurements.

Samuel Wonfor (PhD Candidate), Georgia Tech: Fuel PLIF measurements.

Andrew Zheng (PhD Candidate), Georgia Tech: TiRe-LII processing.

Sundar Ram Manikandan (MS Candidate), Georgia Tech: Thermophoretic nvPM sampling system.

Kailey Obenstine, Coleman Pethel, Rachel Thomas (BS Students), Georgia Tech: Assistance in data processing, burner calibration, diagnostic design, etc.

Plans for Next Period

- Complete data processing from Campaign 1 (Q1 2022)
- Complete Campaign 2 test rig design, fabrication, and assembly (Q1 2022)
- Implement Experimental Campaign 2 (Q2–3 2022)
- Perform data analysis for Campaign 2 (Q3–4 2022)

Task 2 – Large Eddy Simulations of Combustor Operation and Emissions

Georgia Institute of Technology

Objective(s)

Simulations of advanced propulsion and power systems require treatment of multiscale physics, which in turn require trade-offs between cost and accuracy. Achieving the optimal balance is complicated because of the nonlinear nature of turbulent reacting flows, which involve multiphase mixtures, highly nonlinear chemical kinetics, multiscale velocity and mixing processes, turbulence–chemistry interactions, compressibility effects (density changes induced by changes in pressure), and variable inertia effects (density changes induced by changes in composition or heat addition). Coupling between processes occurs over a wide range of time and length scales, with many scales being too small to be resolved in a numerically feasible manner. Further complications arise when liquid or solid phases are present due to the introduction of dynamically evolving interface boundaries and the resultant complex exchange processes.

The overarching objective of this task is to provide quantitative insights into the accuracy of select calculations and to assess critical trade-offs between cost and accuracy. One set of calculations is performed using preferred engineering LES solvers with the goal of minimizing cost for a targeted accuracy, as required by industry. A companion set of high-resolution LES calculations are performed using a research solver, the RAPTOR code at Georgia Tech (Oefelein, 2006; Oefelein & Sankaran, 2018), to provide detailed information beyond that available from experiments alone. Complementary information from the first-principles LESs and experimentally measured data provides a unique opportunity to understand the central physics of turbulent combustion processes in realistic parameter spaces and for making clear assessments of how a given combination of affordable engineering-based models performs. After achieving an adequate level of validation, results from the high-resolution LES calculations will provide fundamental information that cannot be measured directly and that is relevant to the development of lower-order engineering models. Thus, a strong link between theory, experiments, and relevant applications will be established. The ultimate objectives of this task are to assess (a) the model fidelity/attributes required to accurately simulate operability and emissions and (b) the trade-offs between accuracy and cost.

Research Approach

The GE combustor operates with liquid Jet A (CAT-A2) fuel delivered through upstream atomizers into bluff-body stabilized premixers, as well as through a central swirling pilot. Over the initial stages of the project in Year 1, the GE and GT simulation teams worked toward developing a common computational domain that enabled detailed treatment and analysis of rig boundary conditions and operating conditions while also working around proprietary information within GE. A set of calculations was performed by GE using Fluent via standard practice in a computational domain that included the upstream plenum, upstream proprietary liquid-fuel/air injection system, combustion chamber, and exhaust, as shown in Figure 17.

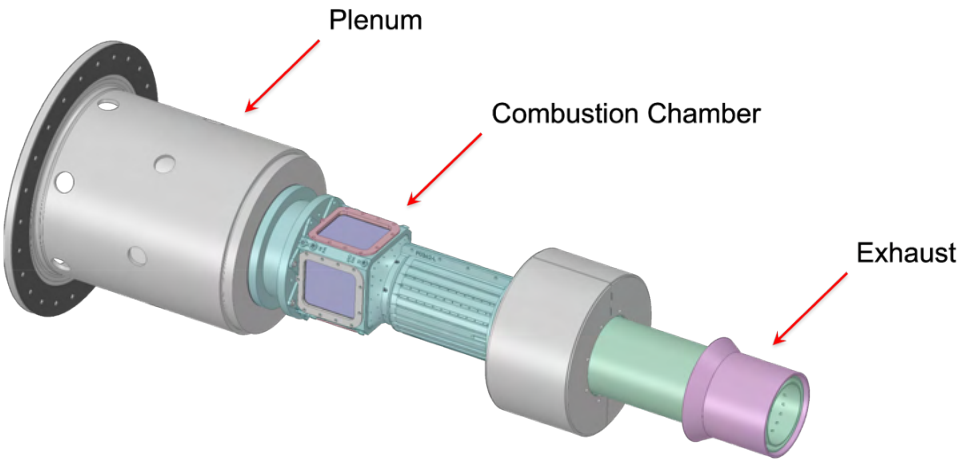

Figure 17. Extended computational domain used for GE Fluent calculations.

In contrast, the GT LES computational domain begins at the burner inlet planes, starting upstream of the dome that houses the bluff-body stabilized premixers, as shown in Figure 18. The domain includes all flow features of the pilot and premixers as well as fine features such as wall and dome cooling holes. The major goals of this effort are to (1) establish good correspondence between the GE and GT simulation efforts, (2) develop advanced methodologies for the treatment of boundary conditions in "industrial grade" rigs such as this, and (3) quantify and enable detailed analyses of both the inner combustion characteristics and the actual physical boundary conditions on the overall operating characteristics of the combustor.

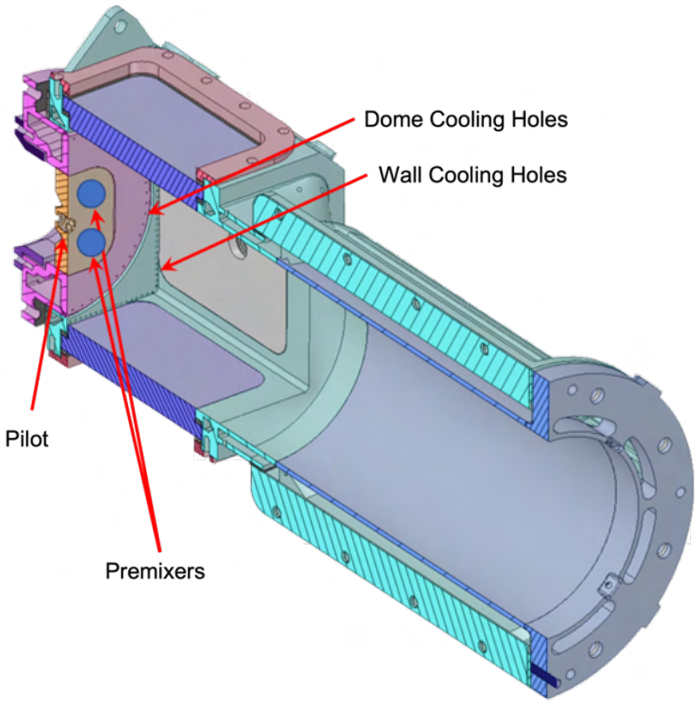

Figure 18. Computational domain used for GT LES calculations.

The simulations performed by GT and GE are complementary, not redundant. GT is performing high-resolution "first-principles" LESs designed to provide additional levels of information that are directly relevant to assessing, understanding, and improving the current state-of-the-art models being used (i.e., detailed treatment of broadband turbulent reacting flow dynamics with an emphasis on accuracy over cost). The GE Fluent calculations are designed to apply "best-practices" engineering CFD to first establish the benchmark accuracy of the current models used and to then systematically assess where improvements can be made to quantify and improve the accuracy of the models under the conditions of interest. The combination of GT and GE calculations will enable an advanced engineering workflow that systematically improves the accuracy and confidence of the CFD design methodology while minimizing cost.

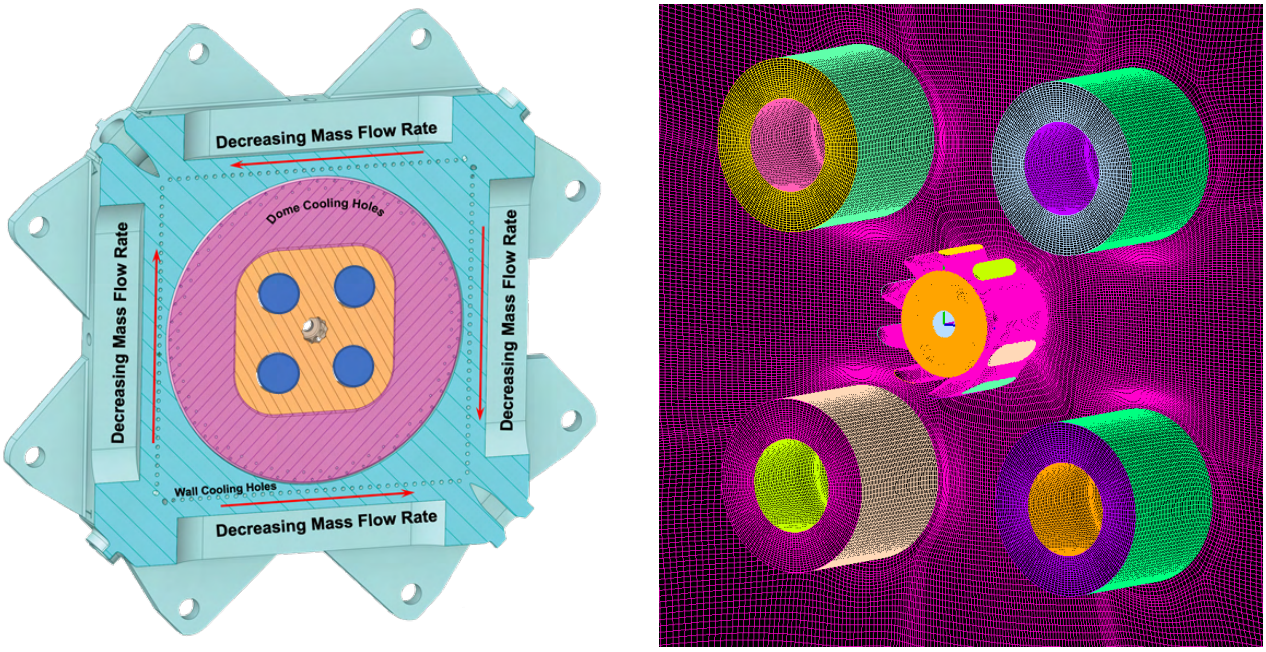

Figure 19. Left: Combustor dome showing key boundary features. Right: A corresponding grid of the back plane of the dome showing inflow planes for the premixer and pilot swirler vanes.

Over this period, we have established the workflow required to quantify the multifidelity treatment of boundary conditions associated with the combustor. This step is essential to assess the impact on operational characteristics of the burner and to unify comparisons of results between different simulation techniques and measured data. The flow entering the combustion chamber involves a complex combination of turbulent gas-phase fluid dynamics and liquid-fuel spray dynamics. The premixers inject partially premixed gas laden with liquid-fuel droplets. The pilot injects radially directed swirling air flow onto a centered liquid-fuel jet. The gas-phase flow velocity and liquid-fuel droplet size and velocity distributions are found to be nonuniform both within and between the premixers. In addition, the mass flow of air through the dome and wall cooling holes makes up 40% of the mass flow, and flow across the wall cooling holes is nonuniform. All of these factors must be considered to establish an advanced quantitative understanding of the combustor while also enabling a unified

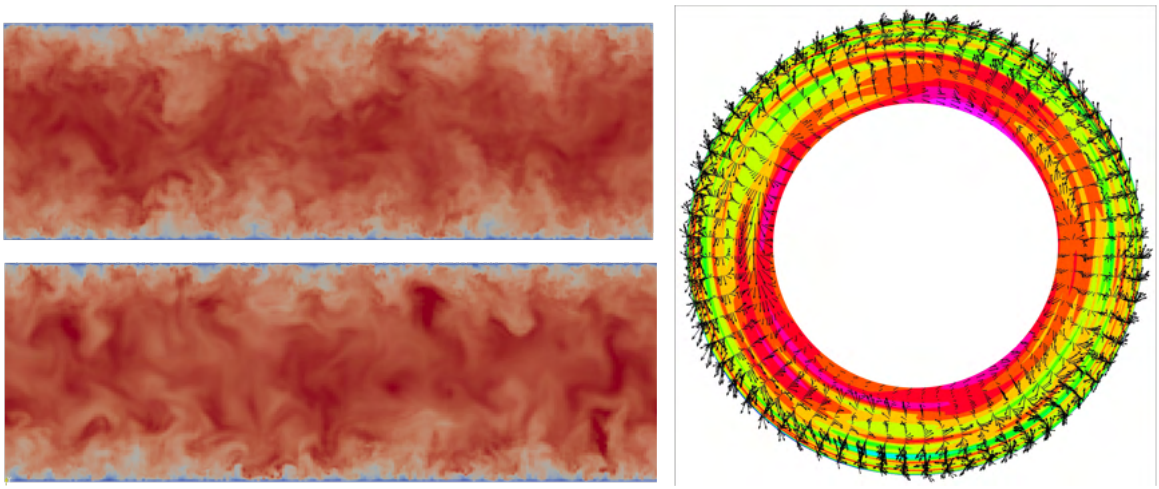

Correlated, fully-coupled, time-evolving, multiphase inflow condition with identical statistics

Figure 20. Left: Comparison of a reconstructed SEM signal (bottom) to the actual NS-generated signal (top) in a turbulent channel flow. Right: Example of the signal generated for one of the premixer planes in the actual combustor reconstructed using data from GE Fluent calculations.

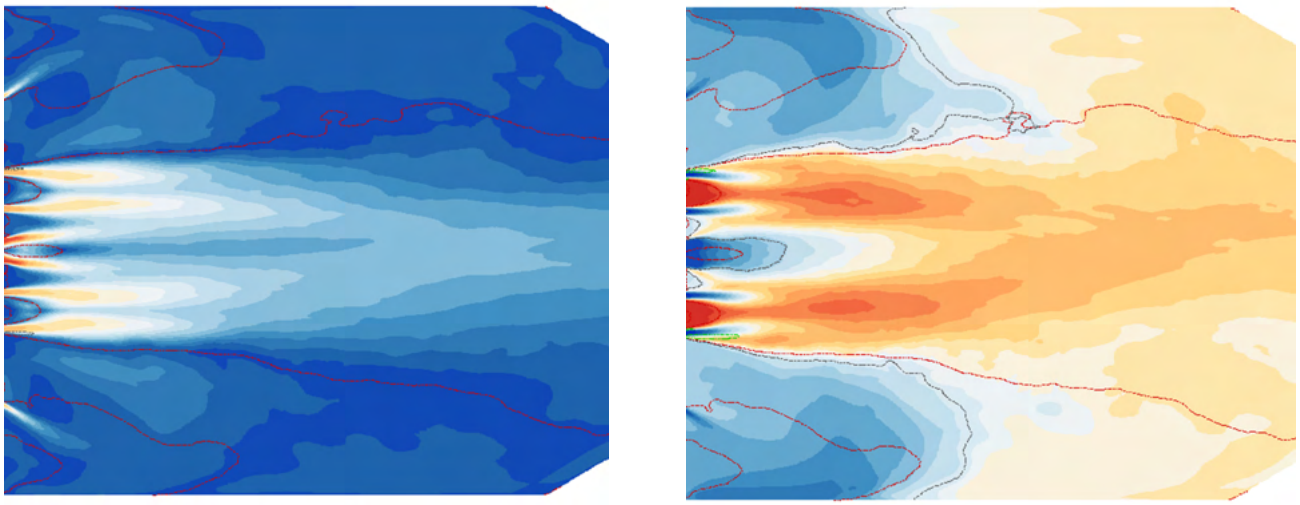

Figure 21. Example simulation results showing the velocity (left) and temperature (right) fields in the combustor.

correspondence between measured and modeled results and comparisons between different simulation methods and models. The current workflow enables a systematic application of complex boundary conditions.

As an example of new developments, we have established an advanced methodology to accurately extract information from the GE calculations, including the upstream plenum and proprietary liquid-fuel/air injection system, which we are not able to access, and to convert this information to unsteady time-correlated boundary conditions at the inlet planes to the premixers, pilot, and wall cooling holes (see Figure 19). Time-dependent turbulent inflow profiles are constructed using the synthetic eddy method (SEM) (Jarrin et al., 2008). A modified compressible SEM formulation is employed to provide time-evolving turbulent inflow conditions to capture the physical nonuniformities present across the premixer inlet planes. The input used to construct the signals includes the nonuniform mean velocity profiles, Reynolds stress tensor, and integral scale distributions extracted at respective planes from the GE Fluent calculations. Figure 20 shows examples of the fidelity in the signals obtained. The left figure presents a comparison of a reconstructed SEM signal to the actual DNS-generated signal in a turbulent channel flow. The right figure shows an example of the signal generated for one of the premixer planes in the actual combustor, reconstructed using data from the GE Fluent calculations. Similar treatments were applied to obtain the nonuniform droplet size, temperature, and species distributions.

Following these detailed characterizations related to the geometry and boundary conditions, simulations are now in progress. An example result is shown in Figure 21. The complexity of the combustor geometry required careful creation of a high-resolution grid that is tractable for computation. The computational domain is meshed with a grid of 45 million (M) grid points over 2,060 structured blocks, with a minimum cell size of 0.058 mm at the inlet (dump) plane of the combustor. The current resolution provides the capability to resolve small-scale flame dynamics at the dump plane. There are three versions of the grid at increasing resolutions of 45 M, 94 M, and 132 M grid points, respectively, which will facilitate multiresolution studies. The tasks in Year 2 will shift toward detailed analyses of combustor characteristics through collaborative comparisons between measured and modeled data and between engineering (GE) and high-resolution (GT) simulations. Planned studies include analyses of (1) sub-model accuracy and performance in a complex geometric environment, (2) turbulent velocity and scalar mixing, (3) turbulent mixed-mode combustion, (4) finite-rate chemical kinetics and combustion dynamics, (5) emissions and soot generation, and (6) engineering model performance and best practices for model implementation.

Milestone(s)

- GE Fluent LES for initial conditions (complete)
- Baseline GT RAPTOR LES for initial conditions (on schedule for completion in Q4 2021)

Major Accomplishments

- Fluent LES of LPP combustor
- Workflow to align space- and time-dependent boundary conditions between GE Fluent and GT RAPTOR

Publications

None

Outreach Efforts

None

Awards

None

Student Involvement

Sriram Kalathoor (GRA, PhD Candidate), Georgia Tech: Baseline calculations with RAPTOR code.

Plans for Next Period

- GE Fluent LES conditions over experimental match conditions (Q1 2022)
- GT RAPTOR LES for selected conditions (Q2 2022)
- Detailed comparison of RAPTOR LES, Fluent LES, and experimental measurements (Q3-4 2022)

References

Berton, J., J., Huff, J. D., Seidel, J. A., & Geiselhart, K. A. (2020). Supersonic technology concept aeroplanes for environmental studies [Presentation]. AIAA SciTech Forum and Exposition, Orlando, FL.

Chen, Y., Cenker, E., Richardson, D. R., Kearney, S. P., Halls, B. R., Skeen, S. A., Shaddix, C. R., & Guildenbecher, D. R. (2018). Single-camera, single-shot, time-resolved laser-induced incandescence decay imaging. Optics Letters, *43*(21), 5363. https://doi.org/10.1364/ol.43.005363

Hassan, M., Pfaender, H., & Mavris, D. (2020). Design tools for conceptual analysis of future commercial supersonic aircraft [Presentation]. AIAA Aviation Forum, Virtual meeting.

Kharina, A., MacDonald, T., & Rutherford, D. (2018). Environmental performance of emerging supersonic transport aircraft [Presentation]. The International Council on Clean Transportation.

Liu, F., Smallwood, G. J., & Snelling, D. R. (2005). Effects of primary particle diameter and aggregate size distribution on the temperature of soot particles heated by pulsed lasers. Journal of Quantitative Spectroscopy and Radiative Transfer, *93*(1-3), 301–312. https://doi.org/10.1016/j.jqsrt.2004.08.027

Goldlucke, J., Seelig, O., Ipp, W., Schraml, S., & Leipertz, A. (2004). Investigation of In-Cylinder Soot Formation and Exhaust Soot Emission of a Direct Injection SI Engine by Laser-Induced Incandescence (LII) (Measurement PM in Flames). The Proceedings of the International Symposium on Diagnostics and Modeling of Combustion in Internal Combustion Engines, *2004.6*(0), 369–376. https://doi.org/10.1299/jmsesdm.2004.6.369

Kheirkhah, S., Cirtwill, J. D. M., Saini, P., Venkatesan, K., & Steinberg, A. M. (2017). Dynamics and mechanisms of pressure, heat release rate, and fuel spray coupling during intermittent thermoacoustic oscillations in a model aeronautical combustor at elevated pressure. Combustion and Flame, *185*, 319–334. https://doi.org/10.1016/j.combustflame.2017.07.017

Strategic Implementation Plan. (2015, November 12). NASA. https://www.nasa.gov/aeroresearch/strategy

Niedzwiecki, R. W. (1992). Low emissions combustor technology for high-speed civil transport engines (Report No. N94-33481). NASA, Cleveland, OH.

Oefelein, J. C. (2006). Large eddy simulation of turbulent combustion processes in propulsion and power systems. Progress in Aerospace Sciences, *42*(1), 2–37. https://doi.org/10.1016/j.paerosci.2006.02.001

Oefelein, J. C., & Sankaran, R. (2018). Large eddy simulation of reacting flow physics. In K. Antypas & T. Williams (Eds.). *Exascale scientific applications: Programming approaches for scalability, performance, and portability* (231-256). Taylor & Francis, Boca Raton, FL.

Orain, M., Baranger, P., Ledier, C., Apeloig, J., & Grisch, F. (2014). Fluorescence spectroscopy of kerosene vapour at high temperatures and pressures: potential for gas turbines measurements. Applied Physics B, *116*(3), 729–745. https://doi.org/10.1007/s00340-013-5756-z

Shaddix, C. R., Zhang, J., Schefer, R. W., Doom, J., Oefelein, J. C., Kook, S., Pickett, L. M., & Wang, H. (2010). Understanding and predicting soot generation in turbulent non-premixed jet flames (Report No. SAND2010-7178). Sandia National Laboratories.

Speth, R. L., Eastham, S. D., Fritz, T. M., Sanz-Morére, I., Agarwal, A., Prashanth, P., Allroggen, F., & Barrett, S. R. H. (2021). Global environmental impact of supersonic cruise aircraft in the stratosphere (Report No. NASA/CR-20205009400). NASA, Cleveland, OH.

Vargas, A. M., & Gülder, Ö. L. (2016). A multi-probe thermophoretic soot sampling system for high-pressure diffusion flames. Review of Scientific Instruments, *87*(5), 055101. https://doi.org/10.1063/1.4947509

Speth, R. L., Eastham, S. D., Fritz, T. M., Sanz-Morére, I., Agarwal, A., Prashanth, P., Allroggen, F., & Barrett, S. R. H. (2021). Global environmental impact of supersonic cruise aircraft in the stratosphere (Report No. 20205009400). NASA, Cleveland, OH.